A fast direct solver for scattering from periodic structures with multiple material interfaces in two dimensions

Leslie Greengard [a], Kenneth L. Ho [b], June-Yub Lee [c,*]

[a] *Courant Institute, New York University, New York, NY 10012, United States*
[b] *Department of Mathematics, Stanford University, Stanford, CA 94305, United States*
[c] *Department of Mathematics, Ewha Womans University, Seoul 120-750, Republic of Korea*

A R T I C L E   I N F O

A B S T R A C T

We present a new integral equation method for the calculation of two-dimensional scattering from periodic structures involving *triple-points* (multiple materials meeting at a single point). The combination of a robust and high-order accurate integral representation and a fast direct solver permits the efficient simulation of scattering from fixed structures at multiple angles of incidence. We demonstrate the performance of the scheme with several numerical examples.

1. Introduction

The interaction of acoustic or electromagnetic waves with structured, periodic materials is often complicated by the fact that the scattering geometry involves domains where multiple media meet at a single point. Examples include the design of diffraction gratings, the development of high efficiency solar cells, and nondestructive optical inspection in semiconductor manufacturing (metrology) [4,12,17,48,57,64,65]. The geometry of a typical scattering problem is shown in Fig. 1.

For the sake of concreteness, we will assume throughout this paper that the governing equations are the Maxwell equations in two dimensions (here, the xy plane). We also assume the incident wave is in TM-polarization [16,38] and that each of the constituent materials is locally isotropic with constant permittivity ϵ and permeability μ. In this case, the Maxwell equations are well-known to take the simpler form

$$\mathbf{E}(x, y, z) = \mathbf{E}(x, y) = \big(0, 0, E(x, y)\big),$$

$$\mathbf{H}(x, y, z) = \mathbf{H}(x, y) = \frac{1}{i\omega\mu}\big(E_y(x, y), -E_x(x, y), 0\big),$$

with

$$\nabla^2 E(\mathbf{x}) + k^2(\mathbf{x})E(\mathbf{x}) = 0 \quad \text{for } \mathbf{x} = (x, y) \in R^2. \tag{1}$$

Here, $k(\mathbf{x}) = \omega\sqrt{\epsilon(\mathbf{x})\mu(\mathbf{x})}$, where we have assumed a time-dependence of $e^{-i\omega t}$ with $\omega > 0$ the frequency of interest.
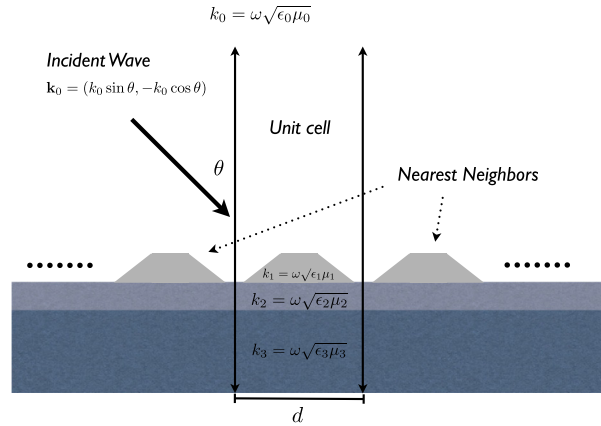
* Corresponding author.

Fig. 1. A periodic array of scatterers on the surface of a layered medium. The Helmholtz coefficient for the upper medium is k_0, that for the trapezoidal-shaped scatterers is k_1 and that of the two layers beneath are k_2 and k_3, respectively. We assume that the lowest interface (here between the k_2 and k_3 layers) is located at $y = 0$ and that the maximum height of the scatterers is at $y = y_0$. We also assume that the unit cell is centered at $x = 0$. The bottom layer is assumed to be infinite in extent.

Using the language of scattering theory, we let

$$E(\mathbf{x}) = u^{in}(\mathbf{x}) + u(\mathbf{x}), \tag{2}$$

where $u^{in}(\mathbf{x})$ is a known incoming field,

$$u^{in}(\mathbf{x}) = u^{in}_{\theta}(x, y) = e^{ik_0(\sin\theta x - \cos\theta y)},$$

and $u(\mathbf{x})$ is the unknown scattered field. At material interfaces,

$$[E] = 0 \quad \Rightarrow \quad [u] = -[u^{in}], \tag{3}$$

$$\left[\frac{1}{\mu}\frac{\partial E}{\partial \nu}\right] = 0 \quad \Rightarrow \quad \left[\frac{1}{\mu}\frac{\partial u}{\partial \nu}\right] = -\left[\frac{1}{\mu}\frac{\partial u^{in}}{\partial \nu}\right], \tag{4}$$

where ν denotes the normal direction and $[f]$ denotes the jump in the quantity f across an interface. For simplicity, we will assume $\mu = 1$ and ϵ is distinct in each domain. The essential difficulties that we wish to address are manifested in that setting, so we ignore other variants of the scattering problem without loss of generality.

Scattering problems of the type illustrated in Fig. 1 are often called *quasi-periodic* since the obstacles are arrayed periodically, but the incoming, scattered and total field experience a phase change in traversing the unit cell:

$$u(x + d, y) = e^{i\alpha d}u(x, y), \tag{5}$$

where $\alpha = k_0 \sin\theta$. (In this convention, normal incidence corresponds to $\theta = 0$.)

In the y-direction, to obtain a well-posed problem, the scattered field u must satisfy a somewhat involved radiation condition [6,7,52,61] – namely that it takes the form of Rayleigh–Bloch expansions

$$u(x, y) = \sum_{n\in\mathbb{Z}} a^+_n e^{i\kappa_n x} e^{ik_n y} \quad y > y_0, \ x \in \mathbb{R}, \tag{6}$$

$$u(x, y) = \sum_{n\in\mathbb{Z}} a^-_n e^{i\kappa_n x} e^{-ik^{(-)}_n y} \quad y < 0, \ x \in \mathbb{R}, \tag{7}$$

assuming, as in Fig. 1, that the lowest interface lies at $y = 0$ and that y_0 is the maximum extent of the scatterers. In this formula, $\kappa_n = k_0 \sin\theta + \frac{2\pi n}{d}$, in order to satisfy the quasi-periodicity condition. Letting $k_n = +\sqrt{k_0^2 - \kappa_n^2}$ enforces that the expansion satisfy the homogeneous Helmholtz equation in the upper half-space, while letting $k^{(-)}_n = +\sqrt{k_l^2 - \kappa_n^2}$ enforces that the expansion satisfy the homogeneous Helmholtz equation in the lower half-space with wavenumber k_l (k_3 in Fig. 1).

Above the scatterers in the unit cell ($y > y_0$), note that if $|\kappa_n| \leqslant k_0$, then k_n is real and the waves in the Rayleigh–Bloch expansion (6) are *propagating* modes. If $|\kappa_n| > k_0$, then k_n is imaginary and the corresponding modes are called *evanescent*. They do not contribute to the far field. See also [56].

Definition 1.1. The complex coefficients a^+_n for propagating modes in the Rayleigh–Bloch expansion are known as the *Bragg diffraction amplitudes at the grating orders*.

For each fixed α and d, there is a discrete set of frequencies ω for which some k_n may vanish, at which point the Rayleigh–Bloch mode is constant in the y-direction. Such modes are called *Wood's anomalies*. (There is also a discrete set of frequencies where the solution is nonunique, due to guided modes which propagate along the grating. The latter are, in a certain sense, nonphysical and we refer the interested reader to [7,44,61] for further discussion.)

In this paper, we present an integral equation method and a corresponding fast direct solver for scattering problems of the type discussed above. We make use of the *quasi-periodic Green's function*, which requires only a discretization of the dielectric interfaces within the unit cell. In a recent paper, Gillman and Barnett [25] address the same problem using a slightly different formulation with a different approach to imposing quasi-periodicity. We will discuss the relative advantages of the two approaches in Section 7.

2. The quasi-periodic Green's function

A classical approach to the calculation of quasi-periodic scattering is based on using the Green's function that satisfies the desired conditions (5), (6), and (7) [3,43,52–54,62]. This is accomplished by constructing a one-dimensional array of suitably "phased" copies of the free-space Green's function for the Helmholtz equation with wavenumber k. More precisely, the quasi-periodic Green's function is defined by

$$G_{\text{QP}}(\mathbf{x}) = G_{\text{QP}}^{(k,\alpha,d)}(\mathbf{x}) = \frac{i}{4} \sum_{m=-\infty}^{\infty} e^{im\alpha d} H_0^{(1)}\big(k|\mathbf{x} - (md, 0)|\big), \tag{8}$$

where $H_0^{(1)}$ is the outgoing Hankel function of order zero. It is clear that the sum formally satisfies the condition (5). The Rayleigh–Bloch conditions (6), (7) follow from Fourier analysis and the fact that $H_0^{(1)}$ itself satisfies the Sommerfeld radiation condition. Unfortunately, the series in (8) is only conditionally convergent for real k. To obtain a physically meaningful limit, one adds a small amount of dissipation ($k \to k + i\epsilon$) and considers $\lim_{\epsilon \to 0} G_{\text{QP}}^{(k+i\epsilon,\alpha,d)}(\mathbf{x})$. (See [6,23] for a more detailed discussion.) We define the "near field" of the quasi-periodic Green's function by

$$G_{\text{QP}}^{\text{near}}(\mathbf{x}) = \frac{i}{4} \sum_{m \in [-1,0,1]} e^{im\alpha d} H_0^{(1)}\big(k|\mathbf{x} - (md, 0)|\big) \tag{9}$$

and the "smooth" part of the quasi-periodic Green's function by

$$G_{\text{QP}}^{\text{far}}(\mathbf{x}) = \frac{i}{4} \sum_{\substack{m \in \mathbb{Z} \\ m \neq [-1,0,1]}} e^{im\alpha d} H_0^{(1)}\big(k|\mathbf{x} - (md, 0)|\big). \tag{10}$$

The latter is a smooth solution to the Helmholtz equation within the unit cell centered at the origin (see Fig. 1) and can be expanded in a Bessel series

$$G_{\text{QP}}^{\text{far}}(\mathbf{x}) = \sum_{n=-\infty}^{\infty} s_n J_n\big(k|\mathbf{x}|\big). \tag{11}$$

In the low frequency regime, where the unit cell is on the order of a few wavelengths or smaller, the Bessel series converges rapidly so long as the y-component of the target point $\mathbf{x}$ is less than d. For larger values of y it is more convenient to switch representations and use the Rayleigh–Bloch expansion (6) directly. An analytic formula for the coefficients s_n of the Bessel expansion (11) can be obtained from the Graf addition theorem [1, Eq. 9.1.79]:

$$s_n = \frac{i}{4} \sum_{\substack{m \in \mathbb{Z} \\ m \neq [-1,0,1]}} e^{im\alpha d} H_n\big(k|md|\big)(-1)^{n \cdot \text{signum}(m)}. \tag{12}$$

These coefficients are known as *lattice sums* and depend only on the parameters k, α, d. Most numerical schemes for the rapid evaluation of the quasi-periodic Green's function are based on the evaluation of

$$G_{\text{QP}}(\mathbf{x}) = \frac{i}{4} \sum_{m \in [-1,0,1]} e^{im\alpha d} H_0^{(1)}\big(k|\mathbf{x} - (md, 0)|\big) + \sum_{n=-\infty}^{\infty} s_n J_n\big(k|\mathbf{x}|\big), \tag{13}$$

combining (9) and (11). There is a substantial literature on efficient methods for computing the lattice sums themselves (see, for example, [23,42,46,49]). In this paper we use a scheme based on asymptotic analysis and the Euler–MacLaurin formula [59]. Since there are a number of effective schemes for this step, we omit further discussion except to note that

1. the quasi-periodic Green's function fails to exist at Wood's anomalies;
2. if the scattering structure in the unit cell has a high aspect ratio $y_0 \gg d$, then the lattice sum approach is inconvenient because more images need to be added to $G_{\text{QP}}^{\text{near}}$ in order to ensure convergence of the Bessel expansion for $G_{\text{QP}}^{\text{far}}$.

We refer the reader to [6,25] for a method capable of handling both these difficulties. Here, we assume that G_{QP} is well-defined and that the aspect ratio y_0/d is less than or equal to 1.

3. The integral equation

In the absence of triple-points, a number of groups have developed high-order accurate integral equation methods for scattering from periodic structures (see, for example, [3,6,11,32,53,64]). For this, suppose that we have a single scatterer Ω in the unit cell, with Helmholtz parameter k_1 and boundary Γ. In the context of Fig. 1, this would correspond to an absence of the layered substrate (that is, $k_2 = k_3 = k_0$), with Ω an isolated trapezoidal-shaped scatterer. One can then use the representation

$$u = \begin{cases} \mathcal{S}^{k_1}[\Gamma, \sigma](\mathbf{x}) + \mathcal{D}^{k_1}[\Gamma, \mu](\mathbf{x}) & \text{in } \Omega, \\ \mathcal{S}_{\text{QP}}^{k_0}[\Gamma, \sigma](\mathbf{x}) + \mathcal{D}_{\text{QP}}^{k_0}[\Gamma, \mu](\mathbf{x}) & \text{in } U \setminus \overline{\Omega}, \end{cases} \tag{14}$$

where $\mathcal{S}$ and $\mathcal{D}$ denote the usual single and double layer operators [20,51,28]

$$\mathcal{S}^k[\Gamma, \sigma](\mathbf{x}) = \int_\Gamma G^k(\mathbf{x} - \mathbf{y}) \sigma(\mathbf{y}) \, ds_{\mathbf{y}}, \tag{15}$$

$$\mathcal{D}^k[\Gamma, \mu](\mathbf{x}) = \int_\Gamma \frac{\partial G^k}{\partial \nu_{\mathbf{y}}}(\mathbf{x} - \mathbf{y}) \mu(\mathbf{y}) \, ds_{\mathbf{y}}, \tag{16}$$

with $G^k(\mathbf{x}) = \frac{i}{4} H_0^{(1)}(k|\mathbf{x}|)$. The quasi-periodic layer potentials $\mathcal{S}_{\text{QP}}^k$ and $\mathcal{D}_{\text{QP}}^k$ are simply defined by replacing the free-space Green's function $G^k(\mathbf{x})$ with $G_{\text{QP}}^k(\mathbf{x})$. Here ds indicates that we are integrating in arclength on Γ, and $\nu_{\mathbf{y}}$ denotes the outward normal at $\mathbf{y} \in \Gamma$. We will also need the normal derivatives of $\mathcal{S}^k$ and $\mathcal{D}^k$ at a point $\mathbf{x} \in \Gamma$, defined by

$$\mathcal{N}^k(\Gamma, \sigma, \mathbf{x}) = \int_\Gamma \frac{\partial G^k}{\partial \nu_{\mathbf{x}}}(\|\mathbf{x} - \mathbf{y}\|) \sigma(\mathbf{y}) \, ds_{\mathbf{y}}, \qquad \mathcal{T}^k(\Gamma, \mu, \mathbf{x}) = \int_\Gamma \frac{\partial^2 G_k}{\partial \nu_{\mathbf{x}} \partial \nu_{\mathbf{y}}}(\|\mathbf{x} - \mathbf{y}\|) \mu(\mathbf{y}) \, ds_{\mathbf{y}}. \tag{17}$$

The periodic versions $\mathcal{N}_{\text{QP}}$ and $\mathcal{T}_{\text{QP}}$ are defined in the same manner. Note that by construction, the governing Helmholtz equation is satisfied in each domain. Note also that we have only chosen to use the quasi-periodic layer potentials in the exterior domain $U \setminus \Omega$. In the context of Fig. 1, we will use the quasi-periodic layer potentials for the k_0, k_2 and k_3 domain and the standard layer potentials for the k_1 domain. $\mathcal{S}^k$ is weakly singular as $\mathbf{x} \to \Gamma$, and the integral is well-defined. For $\mathcal{D}^{(k)}$ and $\mathcal{N}^{(k)}$, the limiting value depends on the side of Γ from which $\mathbf{x}$ approaches the curve. For $\mathbf{x} \in \Gamma$, we assume both are defined in the principal value sense. The operator $\mathcal{T}^{(k)}$ is *hypersingular* and unbounded as a map from the space of smooth functions on Γ to itself. It should be interpreted in the Hadamard finite part sense.

Substituting the representation (14) into the interface conditions (3), (4) and taking the appropriate limits yields the system of integral equations

$$\mu(\mathbf{x}) + \left(\mathcal{S}_{\text{QP}}^{k_0}(\Gamma, \sigma) - \mathcal{S}^{k_1}(\Gamma, \sigma)\right)[\mathbf{x}] + \left(\mathcal{D}_{\text{QP}}^{k_0}(\Gamma, \mu) - \mathcal{D}^{k_1}(\Gamma, \mu)\right)[\mathbf{x}] = -\left[u^{\text{in}}(\mathbf{x})\right], \tag{18a}$$

$$-\sigma(\mathbf{x}) + \left(\mathcal{N}_{\text{QP}}^{k_0}(\Gamma, \sigma) - \mathcal{N}^{k_1}(\Gamma, \sigma)\right)[\mathbf{x}] + \left(\mathcal{T}_{\text{QP}}^{k_0}(\Gamma, \mu) - \mathcal{T}^{k_1}(\Gamma, \mu)\right)[\mathbf{x}] = -\left[\frac{\partial u^{\text{in}}}{\partial \nu}(\mathbf{x})\right] \tag{18b}$$

for the unknowns $[\sigma, \mu]$.

A critical feature of the system (18a), (18b) is that, while $\mathcal{T}$ itself is hypersingular, only the *difference* of hypersingular kernels appears in the equations. All the operators appearing above are compact on smooth domains and we have a system of Fredholm equations of the second kind, for which the formal theory is classical [28,47] and the solution is unique. The cancellation of hypersingular terms in this manner was introduced in electromagnetics by Müller [50], and in the scalar case by Kress, Rokhlin, Haider, Shipman and Venakides [32,41,58].

For smooth domains, the issue of quadrature has been satisfactorily resolved, so that high order accuracy is straightforward to achieve [2,8,33,34,39,40]. The generalized Gaussian quadrature method of [8], for example, permits the use of composite quadrature rules that take into account the singularity of the Green's function and can be stored in tables that do not depend on the curve geometry. Assuming the boundary component Γ is subdivided into Q curved panels with J points on each panel, these rules achieve J-th order accuracy. More precisely, each integral operator

$$\int_\Gamma G^k(\mathbf{x} - \mathbf{y}) \sigma(\mathbf{y}) \, ds_{\mathbf{y}}$$
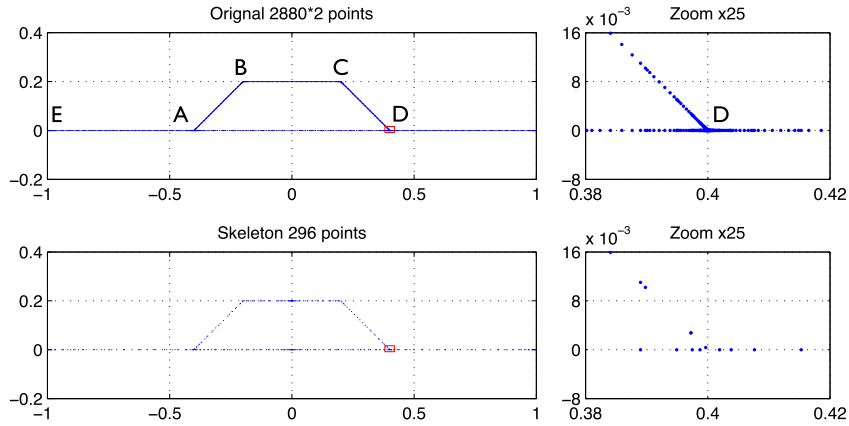
Fig. 2. Discretization points and skeletons for a quasi-periodic scattering problem, where the unit cell consists of a trapezoidal scatterer lying on an infinite substrate. There are six segments with 480 points each and 2 degrees of freedom per point, resulting in a complex matrix of size 5760×5760. After skeletonization, there are only 296 points remaining at the coarsest level of the recursion.

is replaced by a sum of the form

$$\sum_{q=1}^{Q} \sum_{j=1}^{J} \mathcal{G}^k(x_{p,i}, y_{q,j}) \sigma_{q,j} w_{p,i,q,j} \quad \text{for } p = 1, \ldots, Q, \; i = 1, \ldots, J,$$

where $x_{p,i}$ is the i-th Gauss–Legendre node on panel p, $y_{q,j}$ is the j-th Gauss–Legendre node on panel q, $w_{p,i,q,j}$ is a quadrature weight and $\mathcal{G}^k(x_{p,i}, y_{q,j})$ is a "quadrature kernel".

For nonadjacent panels, $\mathcal{G}^k(x_{p,i}, y_{q,j})$ is simply the original kernel $G^k(x_{p,i}, y_{q,j})$. For the interaction of a panel with itself or its two nearest neighbors, the quadrature kernel is produced by a somewhat involved interpolation scheme according to the generalized Gaussian quadrature formalism [8]. From a linear algebra perspective, generalized Gaussian quadrature can be viewed as producing a block tridiagonal matrix (with block size $J \times J$) of interactions of each panel with itself and its two neighbors. These are computed directly. All other block matrix interactions are obtained using standard Gauss–Legendre weights $w_{p,i,q,j} = w_{q,j}$ scaled to the dimensions of the q-th source panel. This structure of the far-field interactions permits the straightforward use of fast multipole acceleration and the hierarchical direct solver of [37].

In domains with corners, but not multi-material junctions, exponentially adaptive grids maintain high-order accuracy (see, for example [10,34]). In the simplest version, one can first divide the boundary into equal size subintervals and employ a J-th order generalized Gaussian quadrature rule on each. For each segment that impinges on a corner point, one can further subdivide it using a dyadically refined mesh, creating $O(\log_2(1/\varepsilon))$ additional subintervals, where $\varepsilon > 0$ is a specified numerical precision. If the same J-th order rule is used for each refined subinterval, it is straightforward to show that the resulting rule has a net error of the order $O(e^{-J} \log_2(1/\varepsilon))$. The need for dyadic refinement comes from the fact that the densities σ or μ may develop singularities at the corner points and the refinement yields a high order piecewise polynomial approximation of the density. For $\varepsilon = 10^{-14}$ and $J = 16$, the net corner error in our experience is about 10^{-14} while for $J = 8$, it is about 10^{-8} (see Fig. 2 for an illustration).

Remark 3.1. In recent work, [10,34] have shown that one can dramatically reduce the number of degrees of freedom in the vicinity of the corner by the use of compression, as well. We have not used such optimization here. See also [5].

It is now appreciated (see, for example [9,33]) that the condition number of a properly discretized system of equations is very well controlled. Following discretization, we use Bremer's approach [9] here, which involves setting the discrete variables to be $\sigma_i \sqrt{w_i}$ and $\mu_i \sqrt{w_i}$, rather than the density values σ_i and μ_i themselves. This ensures that the spectrum of the discrete system approximates the spectrum of the continuous integral equation in L^2. The formal analysis is somewhat involved, since operators that are compact on smooth domains are only bounded (but not compact) on domains with corners. We refer the reader to [9,33] for details.

4. Stable and accurate integral formulations in the presence of multi-material junctions

In the case of multiple subdomains, a natural approach would be to represent the field in each subdomain Ω_i with Helmholtz coefficient k_i in terms of layer potentials on the boundary Γ_i of Ω_i. That is, in subdomain Ω_i, we would represent the solution as

$$u_i(\mathbf{x}) = \mathcal{S}^{k_i}[\Gamma_i, \sigma](\mathbf{x}) + \mathcal{D}^{k_i}[\Gamma_i, \mu](\mathbf{x}), \tag{19}$$

with $\mathcal{S}$ and $\mathcal{D}$ replaced by their quasi-periodic counterparts for subdomains that extend across the unit cell (the k_0, k_2, and k_3 domains in Fig. 1).

In doing so, it turns out that the analog of Eqs. (18a), (18b) fails to converge in the presence of multi-material junctions. The reason for this is simple, and analyzed in [27]. Consider the interface condition (18b) for **x** lying on the segment $\overline{AB}$ in Fig. 2. Restricting our attention just to the segments impinging on the corner point A, we have

$$-\sigma(\mathbf{x}) + \left[\mathcal{N}_{QP}^{k_0}(\overline{AB}, \sigma, \mathbf{x}) - \mathcal{N}^{k_1}(\overline{AB}, \sigma, \mathbf{x}) \right] + \mathcal{N}_{QP}^{k_0}(\overline{AE}, \sigma, \mathbf{x}) - \mathcal{N}^{k_1}(\overline{AD}, \sigma, \mathbf{x}) + \cdots$$

$$+ \left[\mathcal{T}_{QP}^{k_0}(\overline{AB}, \mu, \mathbf{x}) - \mathcal{T}^{k_1}(\overline{AB}, \mu, \mathbf{x}) \right] + \mathcal{T}_{QP}^{k_0}(\overline{AE}, \mu, \mathbf{x}) - \mathcal{T}^{k_1}(\overline{AD}, \mu, \mathbf{x}) + \cdots = -\left[\frac{\partial u^{\text{in}}}{\partial \nu}(\mathbf{x}) \right]. \tag{20}$$

Note that both the terms $\mathcal{T}_{QP}^{k_0}(\overline{AE}, \mu, \mathbf{x})$ and $\mathcal{T}^{k_1}(\overline{AD}, \mu, \mathbf{x})$ involve hypersingular contributions at the junction A without forming part of a difference kernel. This destroys the high-order accuracy of the scheme.

By using a global integral representation, it was shown in [27] that high-order accuracy can be restored. That is, instead of (19), we let

$$u_i(\mathbf{x}) = \mathcal{S}^{k_i}[\Gamma, \sigma](\mathbf{x}) + \mathcal{D}^{k_i}[\Gamma, \mu](\mathbf{x}) \tag{21}$$

and apply the continuity conditions. For $\mathbf{x} \in \Gamma$ lying on an interface between subdomains with Helmholtz coefficients k_i and k_j, we have

$$\mu(\mathbf{x}) + \mathcal{S}^{k_i}(\Gamma, \sigma, \mathbf{x}) - \mathcal{S}^{k_j}(\Gamma, \sigma, \mathbf{x}) + \mathcal{D}^{k_i}(\Gamma, \mu, \mathbf{x}) - \mathcal{D}^{k_j}(\Gamma, \mu, \mathbf{x}) = -\left[\Phi^{\text{in}}(\mathbf{x})\right], \tag{22a}$$

$$-\sigma(\mathbf{x}) + \mathcal{N}^{k_i}(\Gamma, \sigma, \mathbf{x}) - \mathcal{N}^{k_j}(\Gamma, \sigma, \mathbf{x}) + \mathcal{T}^{k_i}(\Gamma, \mu, \mathbf{x}) - \mathcal{T}^{k_j}(\Gamma, \mu, \mathbf{x}) = -\left[\frac{\partial \Phi^{\text{in}}}{\partial \nu}(\mathbf{x})\right]. \tag{22b}$$

As above, the operators $\mathcal{S}$, $\mathcal{D}$, $\mathcal{N}$, $\mathcal{T}$ are replaced by their quasi-periodic counterparts for subdomains that extend across the unit cell (the k_0, k_2, and k_3 domains in Fig. 1).

The global representation (21) is "nonphysical" in the sense that the field in a given subdomain is determined, in part, by layer potential components that are not actually part of the subdomain's boundary. By doing so, however, we remove all hypersingular terms from the integral equation. Only difference kernels appear in the final linear system. One could improve efficiency somewhat, while achieving similar results, by supplementing the representation (19) only by the boundary segments that actually impinge on a multi-material junction. We use the fully global representation in our experiments here for the sake of simplicity.

Remark 4.1. For related approaches addressed at solving problems with multi-material junctions, see [18,19,36].

5. Fast direct solvers

Given a well-conditioned and high order discretization, large scale scattering problems in singular geometries can be solved by using fast multipole-accelerated iterative solution methods such as GMRES [60]. While these are asymptotically optimal schemes, one is often interested in modeling the interaction of a given physical structure (such as the geometry in Fig. 1) with a large number of incoming fields. This requires the solution of an integral equation with multiple right-hand sides, and standard iterative methods do not take maximal advantage of this fact.

Direct solvers, on the other hand, first construct a factorization of the system matrix, then solve against each right-hand side using that factorization at a cost that is typically much lower. In the last decade, specialized versions have been created which are particularly suited to the integral equation environment. This is an active area of research and we do not seek to review the literature, except to note selected important developments in the case of hierarchically semiseparable matrices [13,14,63], $\mathcal{H}$-matrices [29–31], and hierarchically block separable matrices [24,26,37,45]. We provide a brief description of the approach, following the presentation of [24,37].

5.1. Recursive skeletonization for integral equations

Let $\mathsf{A} \in \mathbb{C}^{N \times N}$ be the matrix discretization of an integral equation such as (22), and let its indices $\{1, \ldots, N\}$ be ordered hierarchically according to a quadtree on the unit cell. This can be done by first enclosing the set of all associated points within a sufficiently large box. If the box contains more than a specified number of points, it is subdivided into four quadrants and its points distributed accordingly between them. This procedure is repeated for each new box added, terminating only when all boxes contain $O(1)$ points. The boxes that are not subdivided are called *leaf boxes*. For simplicity, we assume that all leaf boxes live on the same level of the tree, but this restriction can easily be relaxed.

Start at the bottom of the tree and consider the partitioning induced by the leaves. Let p be the number of leaf boxes and assume that each has n points so that $N = pn$. Then A has the block form $\mathsf{A} = \mathsf{A}_{ij}$ for $i, j = 1, \ldots, p$. We now use the *interpolative decomposition* (ID) [15] to skeletonize A. The ID is a matrix factorization that rewrites a given low-rank matrix in terms of a subset of its rows or columns, called *skeletons*. In the integral equation setting, the off-diagonal block rows

$$A_{i\leftarrow} = [A_{i,1}, \ldots, A_{i,i-1}, A_{i,i+1}, \ldots, A_{i,p}] \tag{23}$$

are low-rank due to the smoothness of the Green's function (at least at low to moderate frequencies), and the same is true of the off-diagonal block columns. Thus, it can be shown [24,37] that the ID enables a representation of the form

$$A_{ij} = L_i S_{ij} R_j, \quad i \neq j, \tag{24}$$

for each off-diagonal block, where $L_i \in \mathbb{C}^{n \times q}$, $R_j \in \mathbb{C}^{q \times n}$, and $S_{ij} \in \mathbb{C}^{q \times q}$ is a submatrix of A_{ij}, with $q \ll n$. The matrix can then be written as

$$A = D + LSR, \tag{25}$$

where

$$D = \begin{bmatrix} A_{11} & & 0 \\ & \ddots & \\ 0 & & A_{pp} \end{bmatrix} \in \mathbb{C}^{N \times N}, \qquad L = \begin{bmatrix} L_1 & & 0 \\ & \ddots & \\ 0 & & L_p \end{bmatrix} \in \mathbb{C}^{N \times K}, \qquad R = \begin{bmatrix} R_1 & & 0 \\ & \ddots & \\ 0 & & R_p \end{bmatrix} \in \mathbb{C}^{K \times N}$$

are block diagonal with $K = pq$, and

$$S = \begin{bmatrix} 0 & S_{12} & \cdots & S_{1p} \\ S_{21} & 0 & \cdots & S_{2p} \\ \vdots & \vdots & \ddots & \vdots \\ S_{p1} & S_{p2} & \cdots & 0 \end{bmatrix} \in \mathbb{C}^{K \times K}$$

is dense with zero diagonal blocks.

Remark 5.1. The efficient calculation of the interpolation matrices L_i and R_j, and the associated skeleton indices, in (24) is somewhat subtle. Briefly, it involves separating out neighboring and far-field interactions and representing the latter via free-space interactions with a local "proxy" surface. This is justified by the observation that any well-separated interaction governed by a homogeneous partial differential equation (here, the Helmholtz equation) can be induced by sources/targets on the proxy surface, each of which is expressed in terms of the free-space kernel. For details, see [24,37]. In this paper, for a box of scaled side length 1, we use the circle of radius 1 about the box center as its proxy surface. Note that all neighbors are defined relative to the periodicity of the unit cell.

Now consider the linear system $Ax = b$. One way to solve it is to construct A^{-1} directly from (25) using a variant of the Sherman–Morrison–Woodbury formula. This approach is taken in [24,45]. Here, we follow the strategy of [13,37,55] instead and let $z = Rx$ and $y = Sz$ to obtain the equivalent *sparse* system

$$\begin{bmatrix} D & L & \\ R & & -I \\ & -I & S \end{bmatrix} \begin{bmatrix} x \\ y \\ z \end{bmatrix} = \begin{bmatrix} b \\ 0 \\ 0 \end{bmatrix}. \tag{26}$$

This can be solved efficiently using any standard sparse direct solver and may provide better stability. In this paper, we use the open-source software package UMFPACK [21,22].

Since S is a submatrix of A (up to diagonal modifications), S can itself be expressed in the form (25) by moving up one level in the tree and regrouping appropriately. This leads to a multilevel decomposition

$$A = D^{(\lambda)} + L^{(\lambda)} \left(\cdots D^{(1)} + L^{(1)} D^{(0)} R^{(1)} \cdots \right) R^{(\lambda)}, \tag{27}$$

where the superscript indexes the tree level $l = 0, 1, \ldots, \lambda$ with $l = 0$ denoting the root. We call this process *recursive skeletonization*. The analogue of (26) is

$$\begin{bmatrix} D^{(\lambda)} & L^{(\lambda)} & & & & \\ R^{(\lambda)} & & -I & & & \\ & -I & \ddots & \ddots & & \\ & & \ddots & D^{(1)} & L^{(1)} & \\ & & & R^{(1)} & & -I \\ & & & & -I & D^{(0)} \end{bmatrix} \begin{bmatrix} x^{(\lambda)} \\ y^{(\lambda)} \\ \vdots \\ x^{(1)} \\ y^{(1)} \\ x^{(0)} \end{bmatrix} = \begin{bmatrix} b \\ 0 \\ \vdots \\ 0 \\ 0 \\ 0 \end{bmatrix}, \tag{28}$$

corresponding to expanding S out in the same way. It can be shown that the solver requires $O(N)$ work when the unit cell is a moderate number of wavelengths in size. We refer the reader to [24,37] for further discussion.

For our present purposes, we simply note that the output of the fast direct solver is a *compressed* representation of the inverse which is computed in two steps:

1. a recursive skeletonization procedure to obtain the compressed forward operator (27); and
2. a factorization of the sparse matrix embedding in (28) using UMFPACK.

Both steps have the same asymptotic complexity, but the constant for compression is typically far larger. After the inverse has been computed, it can be applied to each right-hand side as needed at a much lower cost.

Remark 5.2. The ID can be constructed to any specified relative precision $\varepsilon > 0$. This is an input parameter to recursive skeletonization and hence to the direct solver. It can be shown that if (27) has relative error $O(\varepsilon)$, as is often the case numerically, then the algorithm produces a solution with relative error $O(\kappa(\mathsf{A})\varepsilon)$, where $\kappa(\mathsf{A})$ is the condition number of A [35, Theorem 7.2]. In particular, if $\kappa(\mathsf{A}) = O(1)$, as for the integral equation (22), then the error is $O(\varepsilon)$.

Remark 5.3. Although we have assumed in the discussion above that each block at the same level has the same size, this is in no way essential to the algorithm. In fact, our code uses separate "incoming" (row) and "outgoing" (column) skeletons for each box. This enables some additional optimization, which, for the present case, can be especially pronounced. This is because while each point receives incoming interactions from only the two wavenumbers on either side of the segment to which it belongs, it sends outgoing interactions consisting of all wavenumbers in the problem. For example, for a point on the segment $\overline{AB}$ in Fig. 2, it receives at wavenumbers k_0 and k_1 but sends at wavenumbers k_0, k_1, and k_2. Therefore, the outgoing skeleton dimension is typically larger, and the amount by which it is larger increases with the total number of wavenumbers/domains.

5.2. Multiple angles of incidence

The fast direct solver of the previous subsection allows the robust and accurate solution of

$$\mathsf{A}(\theta)\mathsf{x}(\theta) = \mathsf{b}(\theta), \tag{29}$$

where we have made explicit the dependence of the integral equation (22) on the incident angle θ. In the present setting, we are interested in solving (29) for many θ. This is not a situation that the direct solver can easily handle since $\mathsf{A}(\theta)$ is not fixed. In this subsection, we describe a modified strategy for computing a compressed representation (27) of $\mathsf{A}(\theta)$ such that it can be rapidly updated to yield a compressed representation of $\mathsf{A}(\theta')$ for any θ' *without having to re-skeletonize*. Since skeletonization is typically the most expensive step, this can offer significant computational savings. The sparse matrix in (28) must still be updated and re-factored, but the relative cost of this is small.

To see why such a uniform skeletonization might be possible, consider any finite truncation of the periodic geometry so that it consists merely of a very large array of many, many scatterers. Then the governing integral equation is specified in terms of the *free-space* Green's function so that A is independent of θ. The only angle dependence comes from the incoming data $\mathsf{b}(\theta)$. Therefore, only one skeletonized representation of A is needed for all θ. The same is true of any finite approximation to the periodic problem.

We now make this intuition precise by considering all interactions, say, incoming on a given box. This is given by the off-diagonal block row (23) and can be decomposed as

$$\mathsf{A}_{i\leftarrow}(\theta) = \mathsf{A}_{i\leftarrow}^{\text{near}}(\theta) + \mathsf{A}_{i\leftarrow}^{\text{far}}(\theta)$$

in terms of the near- and far-field contributions, respectively, to the quasi-periodic Green's function

$$G_{\text{QP}}(\mathbf{x}; \theta) = G_{\text{QP}}^{\text{near}}(\mathbf{x}; \theta) + G_{\text{QP}}^{\text{far}}(\mathbf{x}; \theta),$$

following Section 2. Clearly, an interpolation basis for both terms together provides an interpolation basis for the sum, so $\mathsf{A}_{i\leftarrow}(\theta)$ can be skeletonized by applying the ID to the rows of the matrix

$$\tilde{\mathsf{A}}_{i\leftarrow}(\theta) = \left[\mathsf{A}_{i\leftarrow}^{\text{near}}(\theta), \; \mathsf{A}_{i\leftarrow}^{\text{far}}(\theta)\right].$$

Since $G_{\text{QP}}^{\text{far}}$ consists only of well-separated interactions, by Remark 5.1, $\mathsf{A}_{i\leftarrow}^{\text{far}}(\theta)$ can be replaced by a matrix $\mathsf{A}_{i\leftarrow}^{\text{proxy}}$ corresponding to free-space interactions with a proxy surface. In linear algebraic terms, this means that $\mathsf{A}_{i\leftarrow}^{\text{far}}$ can be written as $\mathsf{A}_{i\leftarrow}^{\text{far}} = \mathsf{A}_{i\leftarrow}^{\text{proxy}}\mathsf{T}_{i\leftarrow}(\theta)$ for some matrix $\mathsf{T}_{i\leftarrow}(\theta)$. Hence,

$$\tilde{\mathsf{A}}_{i\leftarrow}(\theta) = \begin{bmatrix} \mathsf{A}_{i\leftarrow}^{\text{near}}(\theta) & \mathsf{A}_{i\leftarrow}^{\text{proxy}} \end{bmatrix} \begin{bmatrix} \mathsf{I} & \\ & \mathsf{T}_{i\leftarrow}(\theta) \end{bmatrix}, \tag{30}$$

so $\tilde{\mathsf{A}}_{i\leftarrow}(\theta)$ can be skeletonized by applying the ID to just the left matrix on the right-hand side. Observe that the angular dependence of the far field has been eliminated.

To eliminate the angular dependence of the near field, we can similarly expand $G_{\text{QP}}^{\text{near}}$ in terms of a θ-independent basis. This can be done using the functions

$$\frac{i}{4}H_0^{(1)}\big(k|\mathbf{x}|\big), \qquad \frac{i}{4}H_0^{(1)}\big(k|\mathbf{x}-(d,0)|\big), \qquad \frac{i}{4}H_0^{(1)}\big(k|\mathbf{x}+(d,0)|\big)$$

corresponding to interactions with the self-, left-, and right-images, respectively, with corresponding matrices A^{self}, $\mathsf{A}_{i\leftarrow}^{\text{left}}$, and $\mathsf{A}_{i\leftarrow}^{\text{right}}$. Then, from (9),

$$\mathsf{A}_{i\leftarrow}^{\text{near}}(\theta) = \begin{bmatrix} \mathsf{A}^{\text{self}} & \mathsf{A}_{i\leftarrow}^{\text{left}} & \mathsf{A}_{i\leftarrow}^{\text{right}} \end{bmatrix} \begin{bmatrix} \mathsf{I} \\ e^{-i\alpha d}\mathsf{I} \\ e^{i\alpha d}\mathsf{I} \end{bmatrix}, \tag{31}$$

where, recall, $\alpha = k\sin\theta$, so $\mathsf{A}_{i\leftarrow}(\theta)$ can be skeletonized by applying the ID to

$$\tilde{\mathsf{A}}_{i\leftarrow} = \begin{bmatrix} \mathsf{A}^{\text{self}}, & \mathsf{A}_{i\leftarrow}^{\text{left}}, & \mathsf{A}_{i\leftarrow}^{\text{right}}, & \mathsf{A}_{i\leftarrow}^{\text{proxy}} \end{bmatrix}, \tag{32}$$

which we note has no angular dependence. Thus, the interpolation matrices and skeleton indices resulting from compressing (32) are valid for all θ.

The same approach can be used for outgoing interactions and for interactions at each wavenumber. The result is a modified compressed representation

$$\mathsf{A}(\theta) = \mathsf{D}^{(\lambda)}(\theta) + \mathsf{L}^{(\lambda)}\big(\cdots\mathsf{D}^{(1)}(\theta) + \mathsf{L}^{(1)}\mathsf{D}^{(0)}(\theta)\mathsf{R}^{(1)}\cdots\big)\mathsf{R}^{(\lambda)}, \tag{33}$$

where only the $\mathsf{D}^{(l)}(\theta)$ depend on θ. Therefore, to obtain a compressed representation of $\mathsf{A}(\theta')$ for any other θ', it suffices to perform the update $\mathsf{D}^{(l)}(\theta) \mapsto \mathsf{D}^{(l)}(\theta')$ for each l. This, in general, consists only of generating a very small subset of entries of the new matrix and requires $O(N)$ work with a small constant.

In summary, the full algorithm for analyzing multiple incident angles with fast updating is:

1. Compress the matrix $\mathsf{A}(\theta)$ for some initial θ by representing interactions with an angle-independent basis such as (32). This is an expensive recursive skeletonization that only needs to be performed once.
2. Embed the resulting decomposition (33) into the sparse matrix of (28) and solve.
3. For each new angle θ', update the compressed representation (33) via $D^{(l)}(\theta) \mapsto D^{(l)}(\theta')$. Repeat step 2.

Remark 5.4. In our tests, we have often found it unnecessary to decompose $\mathsf{A}_{i\leftarrow}^{\text{near}}(\theta)$ as in (31). Instead, we apply the ID to the left matrix on the right-hand side of (30), which depends on θ but seems to yield results that recover angle independence numerically. This optimization can reduce the constant associated with skeletonization by about a factor of 2.

6. Numerical results

The algorithm presented above has been implemented in Fortran. Each boundary segment (in the piecewise smooth boundary) is first divided into 22 equal subintervals. The first and last intervals are then further subdivided with dyadic refinement toward the corner using 20 subintervals each. Thus, the total number of intervals on each smooth component of the boundary (each side) is 60 and the number of points is 480. We use the 8th order generalized Gaussian quadrature rule of [8] which provides about 8 digits of accuracy for logarithmic singularities and solve the integral equations (22) using recursive skeletonization [24,37] with a tolerance of $\varepsilon = 10^{-9}$. All timing listed below are for a laptop with a 1.7 GHz Intel Core i5 processor.

Remark 6.1. We have investigated the behavior of the integral equation solver on problems for which the solution is known. To construct nontrivial tests, we place singular sources in each of the subdomains Ω_i and define a solution to the Helmholtz equation in Ω_i as the field induced by those sources *not* contained in Ω_i. Corner singularities are induced in the unknown layer potential densities, and this serves as quite a reliable benchmark for the true scattering problem. Eight digits of accuracy are achieved in these tests, consistent with the quadrature error estimates.

Example 1. We set $\omega = 10$, with ϵ chosen so that the Helmholtz coefficient in the upper half-space, the trapezoidal scatterer, and the substrate are $k = 10$, $40\sqrt{2}$, and 30, respectively. The incident angle is 30°. The original matrix of dimension 5760×5760 is compressed to one of dimension 296×309. The incoming and outgoing skeleton dimensions are slightly different as explained in Remark 5.3 and computed as part of the recursion. The time for compression in our current implementation was 290 s (while generating the necessary matrix entries required 1219 s). Given the compressed representation, the solution time was 2.46 s. The resulting accuracy of the solution (compared with standard LU factorization) was approximately 10^{-9}. We plot the real part of the total field in Fig. 3. In Fig. 2, we plot both the original set of discretization points and the skeletons that remain at the coarsest level of the recursion.
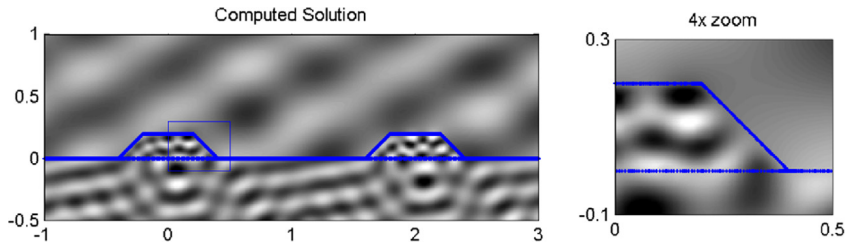
Fig. 3. The real part of the total field when a plane wave at 30° incidence impinges on a periodic structure. The unit cell and its first neighbor are shown, with a zoom in the region of the triple-point.
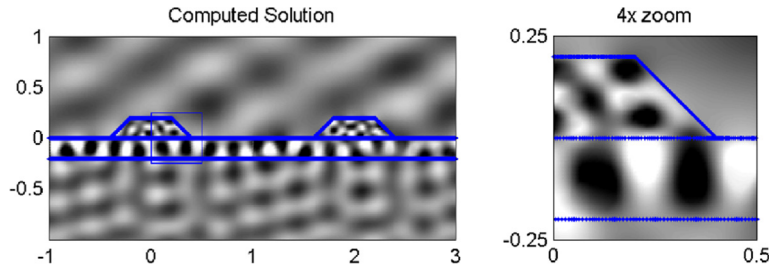

Fig. 4. The real part of the total field when a plane wave at 45° incidence impinges on a periodic structure with a two-layer substrate. The unit cell and its first neighbor are shown, with a zoom in the region of the triple-point.

6.1. Computing the outgoing modes

Given our integral representation of the scattered field, it is straightforward to compute the coefficients a_n^+ in (6) or (7) – the Bragg diffraction amplitudes at the grating orders. For an incident field

$$u^{\text{in}}(\mathbf{x}) = u_\theta^{\text{in}}(x, y) = e^{ik_0(\sin\theta\, x - \cos\theta\, y)},$$

we simply let $y_0 + \delta$ denote some height above the scatterers and rewrite (6) in the form

$$u(x, y_0 + \delta)e^{-k_0\sin\theta\, x} = \sum_{n\in\mathbb{Z}} a_n^+ e^{2\pi inx/d} e^{ik_n(y_0+\delta)},$$

where $k_n = +\sqrt{k_0^2 - (k_0\sin\theta + 2\pi n/d)^2}$. Thus, the $\{a_n^+\}$ can be computed using Fourier analysis:

$$a_n^+ = \frac{1}{d\, e^{ik_n(y_0+\delta)}} \int_0^d u(x, y_0 + \delta)e^{-k_0\sin\theta x}e^{-2\pi inx/d}\, dx.$$

The accurate calculation of a_n^+ from this formula depends on ensuring that the discretization in x is sufficiently fine to resolve the integrand. In the near field (when δ is small), the evanescent modes, corresponding to large n, are still present in $u(x, y_0 + \delta)$ requiring a large number of points to avoid aliasing errors. By making δ sufficiently large, the evanescent modes are suppressed and a mesh can be used that resolves only the propagating modes – that is, values of n for which $(k_0\sin\theta + 2\pi n/d)^2 < k_0^2$.

Example 2. We now consider a scattering problem with a two-layered substrate (Fig. 4). We again set $\omega = 10$ and choose ϵ so that the Helmholtz coefficient in the upper half-space, the trapezoidal scatterer, and the two substrate layers are $k = 10$, $40\sqrt{2}$, 30 and 20, respectively. We first set up the scattering problem for an angle of incidence of 30°. The original matrix is of dimension 7040×7040, which is compressed to one of dimension 422×452. The time for compression was 416.6 s (and for generating the matrix entries, 1762.3 s). The time for inversion was 2.9 s. The relative error in the solution (compared with standard LU factorization) was 1.23×10^{-6}. We then changed the angle of incidence to 45° and used the updating method of Section 5.2. The time for updating the compressed forward operator was 68.4 s and the relative error in the solution was 7.13×10^{-6}. In this problem, there are six propagating modes, with directions indicated in Fig. 5.

Example 3. The complexity of the scattering pattern can be quite striking. The scattering pattern from a semicircular scatterer with an angle of incidence of 30° is illustrated in Fig. 6. We set $\omega = 10$ and choose ϵ so that the Helmholtz coefficient in the upper half-space, the semicircular scatterer and the substrate layer are $k = 30$, $120\sqrt{2}$, and 90, respectively. There are 19 radiation modes at this angle of incidence.

Number of Modes=6, Total Scattered Energy=12.443%
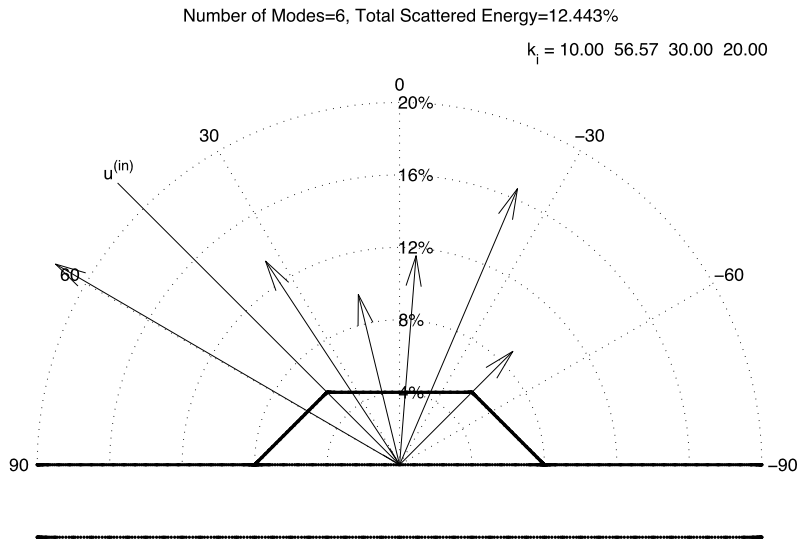
k_i = 10.00 56.57 30.00 20.00

Fig. 5. The strength of the 6 radiation modes in Example 2 corresponding to Fig. 4. The length of the arrows in the various diffraction directions indicate the relative magnitude of the amplitudes a_n^+. Approximately 12.443% of the energy is scattered upward.
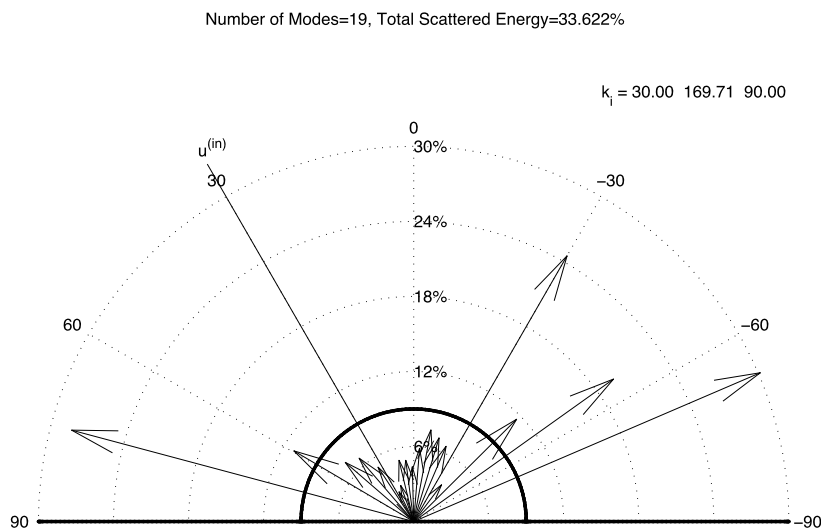
Number of Modes=19, Total Scattered Energy=33.622%

k_i = 30.00 169.71 90.00

Fig. 6. The strength of the 19 radiation modes in Example 3 with a semicircular scatterer with $k_0 = 30$, $k_1 = 120\sqrt{2}$, $k_2 = 90$ and $d = 2$. Only the scatterer in the unit cell is plotted. The length of the arrows in the various diffraction directions indicate the relative amplitudes a_n^+. Approximately 33.622% of the energy is scattered upward.

Examples 4, 5. In our final examples, we compute the diffraction pattern across all angles of incidence from $\theta = -80°$ to $\theta = 80°$ for the scattering geometries depicted in Examples 1 and 3. For the trapezoidal-shaped scatterer, we increased ω over that of Example 1, so that $k_0 = 30$ instead of 10. For the semicircular scatterer, we decreased ω compared to that used in Example 3, so that $k_0 = 10$ instead of 30. On the left-hand side of Figs. 7 and 8 are plotted the diffraction orders as a function of incident angle. That is, for each incident angle θ, the intersection of the indicated vertical line with the various curves are the *Bragg angles* $\theta_n = \tan^{-1}(k_n/\kappa_n)$ according to formula (6), where k_n and κ_n are chosen to enforce both quasi-periodicity and the Helmholtz equation.

Remark 6.2. The number of intersections of each vertical line on these left-hand plots defines the precise number of modes for a given angle of incidence. It is easy to see that each of the curves on the left-hand plots traverses the *incident angle–scattered angle* plane continuously (until it disappears), so that we may enumerate the modes unambiguously from the lower left corner to the upper right corner. The labels ("10", "19", "28") in Fig. 7 are drawn on the 10th, 19th, and 28th such curve. The labels ("4", "7", "10") in Fig. 8 are drawn on the 4th, 7th, and 10th such curve.
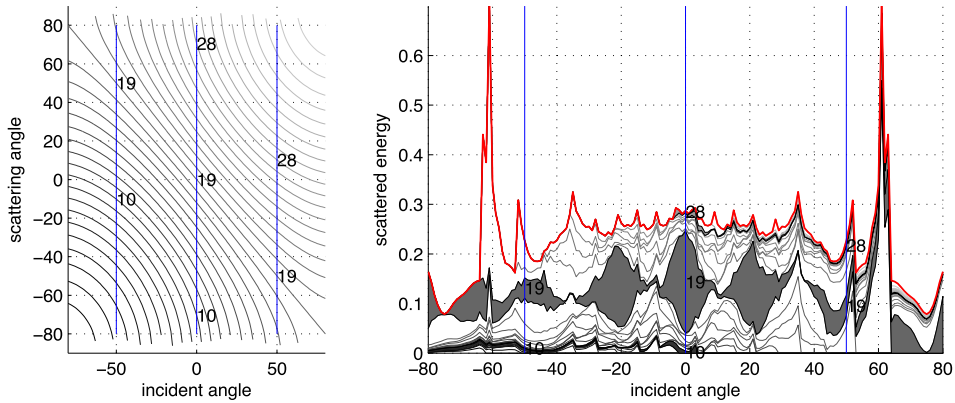
Fig. 7. The Bragg scattering angles as a function of incident angle (left) and the scattering energies in the various modes for the trapezoidal-shaped scatterer shown in Example 1, with $k_0 = 30$. (See the text for a discussion of the plots.)
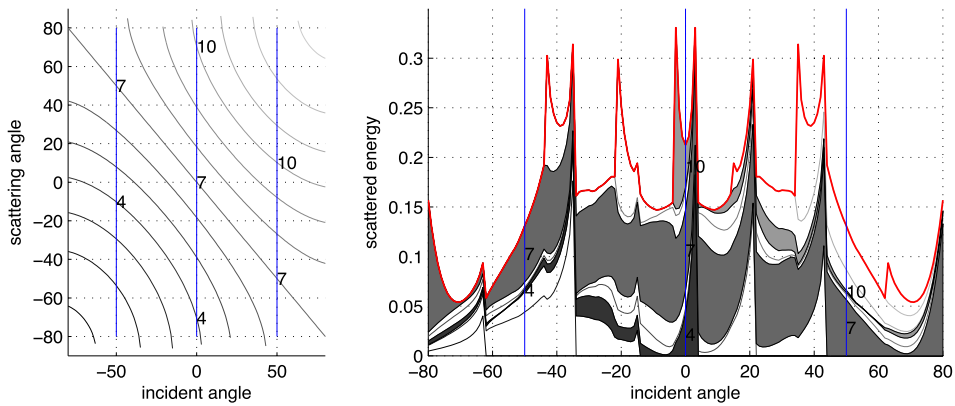

Fig. 8. The Bragg scattering angles as a function of incident angle (left) and the scattering energies in the various modes for the semicircular scatterer of Example 3, with $k_0 = 10$. (See the text for a discussion of the plots.)

On the right-hand side of Figs. 7 and 8 are plotted the fraction of energy radiated into each mode. The ith curve in the right-hand plots show the total energy scattered in modes 1 through i. Thus, the separation between curves corresponding to modes i and $(i-1)$ shows the fraction of energy radiated in the ith mode. Highlighted in gray are the energies scattered in the 10th, 19th, and 28th modes in Fig. 7 and in the 4th, 7th, and 10th modes in Fig. 8. Note that the strength can change quite abruptly when the incident angle is changed only slightly.

7. Conclusions

We have described an integral equation method for quasi-periodic scattering from layered materials with grating-like structures on the "top" surface. It combines (1) the use of the quasi-periodic Green's function, (2) the modified Kress/Müller/Rokhlin integral equation for multi-material junctions [27], (3) the use of exponential refinement near geometric singularities [10,34], and (4) the fast direct solver of [37].

Since the quasi-periodic Green's function changes with each incident angle, there is a global change to the system matrix with each new illumination. We have shown, however, that the *difference* between Green's functions at different angles of incidence is (hierarchically) smooth so that the compressed representation of the system matrix can be rapidly updated.

In recent work, Gillman and Barnett [25] developed an alternative fast direct solver based on using the free-space Green's function with auxiliary variables to impose quasi-periodicity. In that formulation, the bulk of the matrix is left unchanged for different illuminations. Their approach is more flexible with respect to the aspect ratio of the unit cell, but may be more difficult to use in three dimensions. A distinct advantage of the approach of [25] is that it allows for solutions to be computed *at* Wood anomalies. Our solver does not. (In practice, we experienced little difficulty in constructing the Bragg scattering response while sweeping through angles since we never hit the Wood anomalies exactly.) Both approaches have asymptotically optimal complexity for unit cells that are a modest number of wavelengths in size and we suspect that the relative advantages will depend on detailed implementation issues.

Acknowledgements

References

[1] M. Abramowitz, I.A. Stegun, Handbook of Mathematical Functions, Dover, New York, 1965.
[2] B.K. Alpert, Hybrid Gauss–trapezoidal quadrature rules, SIAM J. Sci. Comput. 20 (1999) 1551–1584.
[3] T. Arens, S.N. Chandler-Wilde, J.A. DeSanto, On integral equation and least squares methods for scattering by diffraction gratings, Commun. Comput. Phys. 1 (2006) 1010–1042.
[4] H.A. Atwater, A. Polman, Plasmonics for improved photovoltaic devices, Nat. Mater. 9 (2010) 205–213.
[5] A.H. Barnett, T. Betcke, An exponentially convergent nonpolynomial finite element method for time-harmonic scattering from polygons, SIAM J. Sci. Comput. 32 (2010) 1417–1441.
[6] A. Barnett, L. Greengard, A new integral representation for quasi-periodic scattering problems in two dimensions, BIT 51 (2011) 67–90.
[7] A.-S. Bonnet-BenDhia, F. Starling, Guided waves by electromagnetic gratings and non-uniqueness examples for the diffraction problem, Math. Methods Appl. Sci. 17 (1994) 305–338.
[8] J. Bremer, Z. Gimbutas, V. Rokhlin, A nonlinear optimization procedure for generalized Gaussian quadrature, SIAM J. Sci. Comput. 32 (2010) 1761–1788.
[9] J. Bremer, On the Nyström discretization of integral equations on planar curves with corners, Appl. Comput. Harmon. Anal. 32 (2012) 45–64.
[10] J. Bremer, V. Rokhlin, I. Sammis, Universal quadratures for boundary integral equations on two-dimensional domains with corners, J. Comput. Phys. 229 (2011) 8259–8280.
[11] O.P. Bruno, M.C. Haslam, Efficient high-order evaluation of scattering by periodic surfaces: deep gratings, high frequencies, and glancing incidences, J. Opt. Soc. Am. A 26 (2009) 658–668.
[12] M.E. Carr, E. Topsakal, J.L. Volakis, A procedure for modeling material junctions in 3-D surface integral equation approaches, IEEE Trans. Antennas Propag. 52 (2004) 1374–1379.
[13] S. Chandrasekaran, P. Dewilde, M. Gu, W. Lyons, T. Pals, A fast solver for HSS representations via sparse matrices, SIAM J. Matrix Anal. Appl. 29 (2006) 67–81.
[14] S. Chandrasekaran, M. Gu, T. Pals, A fast *ULV* decomposition solver for hierarchically semiseparable representations, SIAM J. Matrix Anal. Appl. 28 (2006) 603–622.
[15] H. Cheng, Z. Gimbutas, P.G. Martinsson, On the compression of low rank matrices, SIAM J. Sci. Comput. 26 (2005) 1389–1404.
[16] W.C. Chew (Ed.), Waves and Fields in Inhomogeneous Media, IEEE Press, New York, 1995.
[17] W.C. Chew, J.-M. Jin, E. Michielssen, J. Song (Eds.), Fast and Efficient Algorithms in Computational Electromagnetics, Artech House, Boston, 2001.
[18] X. Claeys, A single trace integral formulation of the second kind for acoustic scattering, Seminar of Applied Mathematics Research Report No. 2011-14, ETH, 2011.
[19] X. Claeys, Integral formulation of the second kind for multi-subdomain scattering, in: Proc. 10th Int. Conf. on Math. Numer. Aspects of Waves (WAVES 2011), Pacific Institute for the Mathematical Sciences, 2011, in press, http://www.pims.math.ca/.
[20] D. Colton, R. Kress, Integral Equation Methods in Scattering Theory, Wiley, New York, 1983.
[21] T.A. Davis, Algorithm 832: UMFPACK v4.3—an unsymmetric-pattern multifrontal method, ACM Trans. Math. Softw. 30 (2004) 196–199.
[22] T.A. Davis, I.S. Duff, An unsymmetric-pattern multifrontal method for sparse LU factorization, SIAM J. Matrix Anal. Appl. 18 (1997) 140–158.
[23] A. Dienstfrey, F. Hang, J. Huang, Lattice sums and the two-dimensional, periodic Green's function for the Helmholtz equation, Proc. R. Soc. Lond. A 457 (2001) 67–85.
[24] A. Gillman, P. Young, P.G. Martinsson, A direct solver with $O(N)$ complexity for integral equations on one-dimensional domains, Front. Math. China 7 (2012) 217–247.
[25] A. Gillman, A. Barnett, A fast direct solver for quasi-periodic scattering problems, J. Comput. Phys. 248 (2013) 309–322.
[26] L. Greengard, D. Gueyffier, P.-G. Martinsson, V. Rokhlin, Fast direct solvers for integral equations in complex three-dimensional domains, Acta Numer. 18 (2009) 243–275.
[27] L. Greengard, J.-Y. Lee, Stable and accurate integral equation methods for scattering problems with multiple material interfaces in two dimensions, J. Comput. Phys. 231 (2012) 2389–2395.
[28] R.B. Guenther, J.W. Lee, Partial Differential Equations of Mathematical Physics and Integral Equations, Prentice–Hall, Englewood Cliffs, NJ, 1988.
[29] W. Hackbusch, A sparse matrix arithmetic based on $\mathcal{H}$-matrices. Part I: Introduction to $\mathcal{H}$-matrices, Computing 62 (1999) 89–108.
[30] W. Hackbusch, S. Börm, Data-sparse approximation by adaptive $\mathcal{H}^2$-matrices, Computing 69 (2002) 1–35.
[31] W. Hackbusch, B.N. Khoromskij, A sparse $\mathcal{H}$-matrix arithmetic. Part II: Application to multi-dimensional problems, Computing 64 (2000) 21–47.
[32] M.A. Haider, S.P. Shipman, S. Venakides, Boundary-integral calculations of two-dimensional electromagnetic scattering in infinite photonic crystal slabs: Channel defects and resonances, SIAM J. Appl. Math. 62 (2002) 2129–2148.
[33] J. Helsing, Integral equation methods for elliptic problems with boundary conditions of mixed type, J. Comput. Phys. 228 (2009) 8892–8907.
[34] J. Helsing, R. Olaja, Corner singularities for elliptic problems: integral equations, graded meshes, and compressed inverse preconditioning, J. Comput. Phys. 227 (2008) 8820–8840.
[35] N.J. Higham, Accuracy and Stability of Numerical Algorithms, SIAM, Philadelphia, 2002.
[36] R. Hiptmair, C. Jerez-Hanckes, Multiple traces boundary integral formulation for Helmholtz transmission problems, Adv. Comput. Math. 37 (2012) 39–91.
[37] K.L. Ho, L. Greengard, A fast direct solver for structured linear systems by recursive skeletonization, SIAM J. Sci. Comput. 35 (2012) A2507–A2532.
[38] J.D. Jackson, Classical Electrodynamics, Wiley, New York, 1975.
[39] A. Kloeckner, A. Barnett, L. Greengard, M. O'Neil, Quadrature by expansion: A new method for the evaluation of layer potentials, J. Comput. Phys. 252 (2013) 332–349.
[40] R. Kress, Boundary integral equations in time-harmonic acoustic scattering, Math. Comput. Model. 15 (1991) 229–243.
[41] R. Kress, G. Roach, Transmission problems for the Helmholtz equation, J. Math. Phys. 19 (1978) 1433–1437.
[42] C.M. Linton, The Green's function for the two-dimensional Helmholtz equation in periodic domains, J. Eng. Math. 33 (1998) 377–402.
[43] C.M. Linton, Lattice sums for the Helmholtz equation, SIAM Rev. 52 (2010) 630–674.

[44] C.M. Linton, I. Thompson, Resonant effects in scattering by periodic arrays, Wave Motion 44 (2007) 165–175.
[45] P.-G. Martinsson, V. Rokhlin, A fast direct solver for boundary integral equations in two dimensions, J. Comput. Phys. 205 (2005) 1–23.
[46] R.C. McPhedran, N.A. Nicorovici, L.C. Botten, K.A. Grubits, Lattice sums for gratings and arrays, J. Math. Phys. 41 (2000) 7808–7816.
[47] S.G. Mikhlin, Integral Equations, Pergamon Press, London, 1957.
[48] R. Model, A. Rathsfield, H. Gross, M. Wurm, B. Bodermann, A scatterometry inverse problem in optical mask metrology, J. Phys. Conf. Ser. 135 (2008) 012071.
[49] A. Moroz, Exponentially convergent lattice sums, Opt. Lett. 26 (2001) 1119–1121.
[50] C. Müller, Foundations of the Mathematical Theory of Electromagnetic Waves, Springer-Verlag, Berlin, New York, 1969.
[51] J.-C. Nédélec, Acoustic and Electromagnetic Equations, Springer-Verlag, New York, 2001.
[52] J.-C. Nédélec, F. Starling, Integral equation methods in a quasi-periodic diffraction problem for the time-harmonic Maxwell's equations, SIAM J. Math. Anal. 22 (1991) 1679–1701.
[53] M.J. Nicholas, A higher order numerical method for 3-D doubly periodic electromagnetic scattering problems, Commun. Math. Sci. 6 (2008) 669–694.
[54] Y. Otani, N. Nishimura, A periodic FMM for Maxwell's equations in 3D and its applications to problems related to photonic crystals, J. Comput. Phys. 227 (2008) 4630–4652.
[55] T.P. Pals, Multipole for scattering computations: spectral discretization, stabilization, fast solvers, PhD thesis, Department of Electrical and Computer Engineering, University of California, Santa Barbara, 2004.
[56] R. Petit (Ed.), Electromagnetic Theory of Gratings, Topics in Current Physics, vol. 22, Springer-Verlag, Heidelberg, 1980.
[57] J.M. Putnam, L.N. Medgyesi-Mitschang, Combined field integral equation for inhomogeneous two- and three-dimensional bodies: The junction problem, IEEE Trans. Antennas Propag. 39 (1991) 667–672.
[58] V. Rokhlin, Solution of acoustic scattering problems by means of second kind integral equations, Wave Motion 5 (1983) 257–272.
[59] R. Denlinger, Z. Gimbutas, L. Greengard, V. Rokhlin, A numerical method for the evaluation of lattice sums using the Euler–MacLaurin formula, in preparation.
[60] Y. Saad, M.H. Schultz, GMRES: a generalized minimum residual algorithm for solving nonsymmetric linear systems, SIAM J. Sci. Stat. Comput. 7 (1986) 856–869.
[61] S. Shipman, Resonant scattering by open periodic waveguides, in: Progress in Computational Physics (PiCP), vol. 1, Bentham Science Publishers, Dubai, 2010, pp. 7–49.
[62] S. Venakides, M.A. Haider, V. Papanicolaou, Boundary integral calculations of two-dimensional electromagnetic scattering by photonic crystal Fabry–Perot structures, SIAM J. Appl. Math. 60 (2000) 1686–1706.
[63] J. Xia, S. Chandrasekaran, M. Gu, X.S. Li, Superfast multifrontal method for large structured linear systems of equations, SIAM J. Matrix Anal. Appl. 31 (2009) 1382–1411.
[64] M.S. Yeung, Single integral equation for diffraction from dielectric gratings in layered media, Microw. Opt. Technol. Lett. 32 (2002) 383–388.
[65] P. Yla-Oijala, M. Taskinen, J. Sarvas, Surface integral equation method for general composite metallic and dielectric structures with junctions, Prog. Electromagn. Res. 52 (2005) 81–108.